Inorganic Chemistry
Article

Inorg. Chem. **2009**, *48*, 9579–9591 **9579**
DOI: 10.1021/ic901675p

Relative Binding Affinity of Thiolate, Imidazolate, Phenoxide, and Nitrite Toward the $\{Fe(NO)_2\}$ Motif of Dinitrosyl Iron Complexes (DNICs): The Characteristic Pre-Edge Energy of $\{Fe(NO)_2\}^9$ DNICs

Ming-Che Tsai,[†] Fu-Te Tsai,[†] Tsai-Te Lu,[†] Ming-Li Tsai,[†] Yin-Ching Wei,[†] I-Jui Hsu,*[,‡] Jyh-Fu Lee,[§] and Wen-Feng Liaw*[,†]

[†]*Department of Chemistry, National Tsing Hua University, Hsinchu 30013, Taiwan,* [‡]*Department of Molecular Science and Engineering, National Taipei University of Technology, Taipei 10608, Taiwan, and* [§]*National Synchrotron Radiation Research Center, Hsinchu, Taiwan*

Received August 22, 2009

The synthesis, characterization, and transformation of the anionic $\{Fe(NO)_2\}^9$ dinitrosyl iron complexes (DNICs) $[(NO)_2Fe(ONO)_2]^-$ (**1**), $[(NO)_2Fe(OPh)_2]^-$ (**2**), $[(NO)_2Fe(OPh)(C_3H_3N_2)]^-$ (**3**) ($C_3H_3N_2$=imidazolate), $[(NO)_2Fe(OPh)(\text{-}SC_4H_3S)]^-$ (**4**), $[(NO)_2Fe(p\text{-}OPhF)_2]^-$ (**5**), and $[(NO)_2Fe(SPh)(ONO)]^-$ (**6**) were investigated. The binding affinity of ligands ($[SPh]^-$, $[-SC_4H_3S]^-$, $[C_3H_3N_2]^-$, $[OPh]^-$, and $[NO_2]^-$) toward the $\{Fe(NO)_2\}^9$ motif follows the ligand-displacement series $[SPh]^- \sim [-SC_4H_3S]^- > [C_3H_3N_2]^- > [OPh]^- > [NO_2]^-$. The findings, the pre-edge energy derived from the 1s → 3d transition in a distorted T_d environment of the Fe center falling within the range of 7113.4−7113.8 eV for the anionic $\{Fe(NO)_2\}^9$ DNICs, implicate that the iron metal center of DNICs is tailored to minimize the electronic changes accompanying changes in coordinated ligands. Our results bridging the ligand-substitution reaction study and X-ray absorption spectroscopy study of the electronic richness of the $\{Fe(NO)_2\}^9$ core may point the way to understanding the reasons for nature's choice of combinations of cysteine, histidine, and tyrosine in protein-bound DNICs and rationalize that most DNICs characterized/proposed nowadays are bound to the proteins almost through the thiolate groups of cysteinate/glutathione side chains in biological systems.

Introduction

Dinitrosyliron complexes (DNICs), characterized by their distinctive electron paramagnetic resonance (EPR) signals at $g = 2.03$ in vitro/in vivo, have been suggested as one of the possible forms for storage and transport of NO in biological systems.[1−3] The binding of NO to [Fe−S] cluster-containing proteins or enzymes in mitochondria yielding DNICs and dinuclear $[Fe(\mu\text{-}SR)(NO)_2]_2$ (Roussin's red ester) have been intensely studied.[1,3,4a−4c] In addition, it has been demonstrated that the chelatable iron pool (CIP) is rapidly and quantitatively converted to paramagnetic protein-bound DNICs from the exposure of CIP to free •NO.[4d] Although cysteine and glutathione have been proposed to be the major thiol components of cellular DNICs in vivo,[5] four different kinds of potential coordinated ligands (cysteinate, histidine, deprotonated imidazole, and tyrosinate) in protein-bound DNICs, on the basis of EPR spectra, were proposed in enzymology.[6] Recently, the protein-bound DNIC resulting from the nitrosylation of human glutathione transferase P1−1 by a dinitrosyl diglutathionyliron complex in vitro/in vivo

*To whom correspondence should be addressed. E-mail: wfliaw@mx.nthu.edu.tw (W.-F.L.).

(1) (a) Lancaster, J. R. Jr.; Hibbs J. B. Jr. *Proc. Natl. Acad. Sci. U.S.A.* **1990** *87*, 1223–1227. (b) Foster, M. W.; Cowan, J. A. *J. Am. Chem. Soc.* **1999**, *121*, 4093–4100. (c) Cooper, C. E. *Biochim. Biophys. Acta* **1999**, *1411*, 290–309. (d) Butler, A. R.; Megson, I. L. *Chem. Rev.* **2002**, *102*, 1155–1166. (e) Ueno, T.; Susuki, Y.; Fujii, S.; Vanin, A. F.; Yoshimura, T. *Biochem. Pharmacol.* **2002**, *63*, 485–493. (f) McCleverty, J. A. *Chem. Rev.* **2004**, *104*, 403–418.

(2) (a) Mülsch, A.; Mordvintcev, P. I.; Vanin, A. F.; Busse, R. *FEBS Lett.* **1991**, *294*, 252–256. (b) Badorff, C.; Fichtlscherer, B.; Muelsch, A.; Zeiher, A. M.; Dimmeler, S. *Nitric Oxide* **2002**, *6*, 305–312.

(3) (a) Stamler, J. S.; Singel, D. J.; Loscalzo, J. *Science* **1992**, *258*, 1898–1902. (b) Stamler, J. S. *Cell* **1994**, *78*, 931–936. (c) Frederik, A. C.; Wiegant, I. Y.; Malyshev, I. Y.; Kleschyov, A. L.; van Faassen, E.; Vanin, A. F. *FEBS Lett.* **1999**, *455*, 179–182.

(4) (a) Ding, H.; Demple, B. *Proc. Natl. Acad. Sci. U.S.A.* **2000**, *97*, 5146–5150. (b) Cesareo, E.; Parker, L. J.; Pedersen, J. Z.; Nuccetelli, M.; Mazzetti, A. P.; Pastore, A.; Federici, G.; Caccuri, A. M.; Ricci, G.; Adams, J. J.; Parker, M. W.; Bello, M. L. *J. Biol. Chem.* **2005**, *280*, 42172–42180. (c) Maria, F. D.; Pedersen, J. Z.; Caccuri, A. M.; Antonini, G.; Turella, P.; Stella, L.; Bello, M. L.; Federici, G.; Ricci, G. *J. Biol. Chem.* **2003**, *278*, 42283–42293. (d) Toledo, J. C. Jr.; Bosworth C. A.; Hennon, S. W.; Mahtani, H. A.; Bergonia, H. A.; Lancaster, J. R. Jr. *J. Biol. Chem.* **2008** *283*, 28926–28933.

(5) (a) Lewandowska, H.; Meczynska, S.; Sochanowicz, B.; Sadlo, J.; Kruszewski, M. *J. Biol. Inorg. Chem.* **2007**, *12*, 345–352. (b) Stadler, J.; Bergonia, H. A.; Di Silvio, M.; Sweetland, M. A.; Billiar, T. R.; Simmons, R. L.; Lancaster, J. R. Jr. *Arch. Biochem. Biophys.* **1993** *302*, 4–11.

(6) (a) Kennedy, M. C.; Antholine, W. E.; Beinert, H. *J. Biol. Chem.* **1997**, *272*, 20340–20347. (b) Boese, M.; Mordvintcev, P. I.; Vanin, A. F.; Busse, R.; Mülsch, A. *J. Biol. Chem.* **1995**, *270*, 29244–29249. (c) Lee, M.; Arosio, P.; Cozzi, A.; Chasteen, N. D. *Biochemistry* **1994**, *33*, 3679–3687.

Published on Web 09/11/2009

was characterized by single-crystal X-ray crystallography.[4b] Upon the addition of NO to the [3Fe−4S] form of *m*-aconitase, new transient signals, tentatively assigned as DNICs containing two histidyl ligands or DNICs containing mixed histidine and cysteine ligands, appear during the early phases of the reaction.[6a]

Also known in inorganic chemistry is the precedent for low-molecular-weight DNICs at four oxidation levels, including the EPR-active, anionic/neutral/cationic $\{Fe(NO)_2\}^9$ DNICs as well as the EPR-silent, neutral $\{Fe(NO)_2\}^{10}$ DNICs coordinated by CO, PPh_3, and N-containing ligands.[7−10] Here, the electronic state of the $\{Fe(NO)_2\}$ unit of DNICs is generally designated as $\{Fe(NO)_2\}^n$ (*n* is the total number of electrons associated with the metal d and π^* (NO) orbitals), invoking the Enemark−Feltham notation.[11] Recently, we have established that the IR ν_{NO} in combination with EPR spectra (pattern) may be employed to discriminate between the $\{Fe(NO)_2\}^9$ DNICs with a variety of coordinated ligands (thiolate, imidazole, and imidazolate).[7c,12] Transformations of $[(NO)_2Fe(\mu\text{-}SC_6H_4\text{-}o\text{-}NHCOPh)]_2$ into the neutral $\{Fe(NO)_2\}^{10}$ DNICs $[(NO)_2Fe(PPh_3)_2]$ via reductive elimination of the bridged thiolates and into the anionic $\{Fe(NO)_2\}^9$ $[(NO)_2Fe(SC_6H_4\text{-}o\text{-}NCOPh)]^-$ containing anionic sulfur−amide chelating ligands were elucidated to be controlled by the nucleophile L (L = PPh_3, $[OPh]^-$).[13] In addition, conversion of the EPR-active, anionic $\{Fe(NO)_2\}^9$ DNICs $[(NO)_2Fe(C_3H_3N_2)_2]^-$ ($C_3H_3N_2$ = imidazolate) into the anionic $\{Fe(NO)_2\}^9$ $[(NO)_2Fe(C_3H_3N_2)(SR)]^-$ (R = ^{t}Bu, Et, Ph) via ligand exchange was demonstrated.[12]

Because of the small energy difference between transition-metal d and NO π^* orbitals, it is complicated to define the "noninnocent" character of NO acting as NO^+, NO^-, or NO.[14] Within the class of $Fe(NO)_2\}^9$ DNICs, the oxidation state of iron and NO are in controversy. Intriguingly, a recent investigation of the electronic structure of the $\{Fe(NO)_2\}^9$ unit of complex $[(NO)_2FeS_5]^-$ inferred that $[(NO)_2FeS_5]^-$ is better described as an $\{Fe^I(NO)_2\}^9$ electronic structure related to the spin configuration as "Fe (S = 3/2) antiferromagnetically coupled to two NO (S = 1/2) ligands".[7a] Although some DNICs have been proposed to contain [N,O]/[O,O]-coordinate ligands in enzymology,[6] no mononuclear DNICs coordinated by phenoxide, the mixed phenoxide−imidazolate, and the mixed phenoxide−thiolate have been isolated and characterized in synthetic chemistry. In this manuscript, the synthesis, reactivity, and transformation of the EPR-active, anionic $\{Fe(NO)_2\}^9$ $[(NO)_2Fe(ONO)_2]^-$ (**1**), $[(NO)_2Fe(OPh)_2]^-$ (**2**), $[(NO)_2Fe(OPh)(C_3H_3N_2)]^-$ ($C_3H_3N_2$ = imidazolate) (**3**), $[(NO)_2Fe(OPh)(-SC_4H_3S)]^-$ ($-SC_4H_3S$ = thienylthiolate) (**4**), $[(NO)_2Fe(p\text{-}OPhF)_2]^-$ (**5**), and $[(NO)_2Fe(SPh)(ONO)]^-$ (**6**) are described. The binding affinity of nitrite/phenoxide/imidazolate/thiolate toward the $\{Fe(NO)_2\}^9$ motif was investigated. Also, the present work was undertaken to propose the electronic structure of the $\{Fe(NO)_2\}$ core of $\{Fe(NO)_2\}^9$ DNICs containing the various ligation modes [S,S]/[S,O]/[O,O]/[N,O] on the basis of crystal structure data, EPR spectroscopy, X-ray absorption spectroscopy (XAS) of the Fe K-edge, and DFT computation.

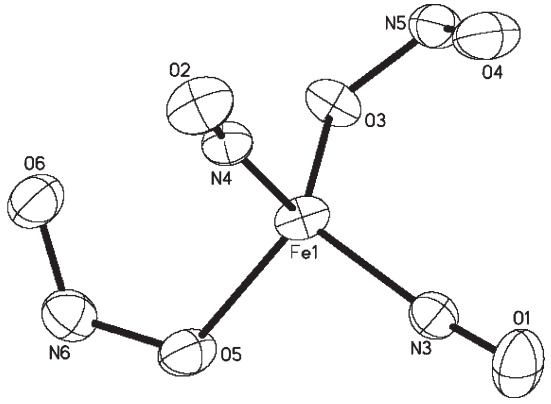

Figure 1. ORTEP drawing and labeling scheme of complex **1** with thermal ellipsoids drawn at 50% probability. Selected bond lengths (Å) and angles (deg): Fe(1)−N(4) 1.691(2), Fe(1)−N(3) 1.699(2), Fe(1)−O(5) 2.002(1), Fe(1)−O(3) 2.038(1), N(3)−O(1) 1.173(2), N(4)−O(2) 1.173(2), N(5)−O(4) 1.236(2), N(5)−O(3) 1.271(2), N(6)−O(6) 1.214(2), N(6)−O(5) 1.303(2), O(1)−N(3)−Fe(1) 161.1(2), O(2)−N(4)−Fe(1) 164.3(2), N(3)−Fe(1)−N(4) 110.3(1), O(4)−N(5)−O(3) 112.9(2), O(6)−N(6)−O(5) 115.0(2), O(3)−Fe(1)−O(5) 93.5(1).

Results and Discussion

Upon the addition of $[PPN][NO_2]$ into a THF solution of complex $[Fe(CO)_2(NO)_2][BF_4]$ in a 2:1 stoichiometry,[15,16] a reaction ensued over the course of 5 min to yield the anionic $\{Fe(NO)_2\}^9$ $[PPN][(NO)_2Fe(ONO)_2]$ (**1**) containing two O-bound nitrito ligands, identified by IR, UV−vis, EPR, and single-crystal X-ray crystallography (Figure 1). Complex **1** is thermally stable in THF solution and exhibits diagnostic IR ν_{NO} stretching frequencies at 1775 s and 1705 s cm^{-1} (THF). The EPR spectrum (Figure 2) of complex **1** displays an isotropic signal with $g = 2.033$ at 298 K and a rhombic signal with $g_1 = 2.052$, $g_2 = 2.029$, and $g_3 = 2.014$ at 77 K, consistent with the characteristic *g* value of $\{Fe(NO)_2\}^9$ DNICs.[7,12,13,15]

In contrast to the decomposition observed in the reaction of $[Fe(CO)_2(NO)_2]^+$ and [Na][OPh] in THF at ambient temperature, the addition of 2 equiv of [Na][OPh] to the

(7) (a) Tsai, M. L.; Chen, C. C.; Hsu, I. J.; Ke, S. C.; Hsieh, C. H.; Chiang, K. A.; Lee, G. H.; Wang, Y.; Liaw, W. F. *Inorg. Chem.* **2004**, *43*, 5159–5167. (b) Tsai, F. T.; Chiou, S. J.; Tsai, M. C.; Tsai, M. L.; Huang, H. W.; Chiang, M. H.; Liaw, W. F. *Inorg. Chem.* **2005**, *44*, 5872–5881. (c) Tsai, M. L.; Liaw, W. F. *Inorg. Chem.* **2006**, *45*, 6583–6585. (d) Hung, M. C.; Tsai, M. C.; Lee, G. H.; Liaw, W. F. *Inorg. Chem.* **2006**, *45*, 6041–6047. (e) Lu, T. T.; Chiou, S. J.; Chen, C. .Y.; Liaw, W. F. *Inorg. Chem.* **2006**, *45*, 8799–8806. (f) Chen, T. N.; Lo, F. C.; Tsai, M. L.; Shih, K. N.; Chiang, M. H.; Lee, G. H.; Liaw, W. F. *Inorg. Chim. Acta* **2006**, *359*, 2525–2533. (g) Chiou, S. J.; Wang, C. C.; Chang, C. M. *J. Organomet. Chem.* **2008**, *693*, 3582–3586. (h) Hsu, I.-J.; Hsieh, C.-H.; Ke, S.-C.; Chiang, K.-A.; Lee, J.-M.; Chen, J.-M.; Jang, L.-Y.; Lee, G.-H.; Wang, Y.; Liaw, W.-F. *J. Am. Chem. Soc.* **2007**, *129*, 1151–1159. (i) Lee, C.-M.; Chen, C.-H.; Dutta, A.; Lee, G.-H.; Liaw, W.-F. *J. Am. Chem. Soc.* **2003**, *125*, 11492–11493.

(8) (a) Chiang, C. Y.; Miller, M. L.; Reibenspies, J. H.; Darensbourg, M. Y. *J. Am. Chem. Soc.* **2004**, *126*, 10867–10874. (b) Baltusis, L. M.; Karlin, K. D.; Rabinowitz, H. N.; Dewan, J. C.; Lippard, S. J. *Inorg. Chem.* **1980**, *19*, 2627–2632.

(9) Albano, V. G.; Araneo, A.; Bellon, P. L.; Chani, G.; Manassero, M. *J. Organomet. Chem.* **1974**, *67*, 413–422.

(10) Reginato, N.; McCrory, C. T. C.; Pervitsky, D.; Li, L. *J. Am. Chem. Soc.* **1999**, *121*, 10217–10218.

(11) Enemark, J. H.; Feltham, R. D. *Coord. Chem. Rev.* **1974**, *13*, 339–406.

(12) Huang, H. W.; Tsou, C. C.; Kuo, T. S.; Liaw, W. F. *Inorg. Chem.* **2008**, *47*, 2196–2204.

(13) Tsai, M. L.; Hsieh, C. H.; Liaw, W. F. *Inorg. Chem.* **2007**, *46*, 5110–5117.

(14) (a) Franz, K. J.; Lippard, S. J. *J. Am. Chem. Soc.* **1998**, *120*, 9034–9040. (b) Brown, C. A.; Pavlosky, M. A.; Westre, T. E.; Zhang, Y.; Hedman, B.; Hodgson, K. O.; Solomen, E. I. *J. Am. Chem. Soc.* **1995**, *117*, 715–732.

(15) Tsai, F. T.; Kuo, T. S.; Liaw, W. F. *J. Am. Chem. Soc.* **2009**, *131*, 3426–3427.

(16) Atkinson, F. I.; Blackwell, H. E.; Brown, N. C.; Connelly, N. G.; Crossley, J. G.; Orpen, A. G.; Rieger, A. L.; Rieger, P. H. *J. Chem. Soc., Dalton Trans.* **1996**, 3491–3502.

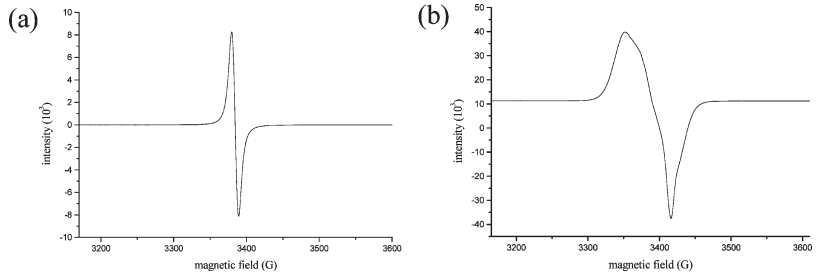

Figure 2. EPR spectrum of complex **1** (a) at 298 K ($g = 2.033$) and (b) at 77 K ($g_1 = 2.052$, $g_2 = 2.029$, and $g_3 = 2.014$).

Scheme 1

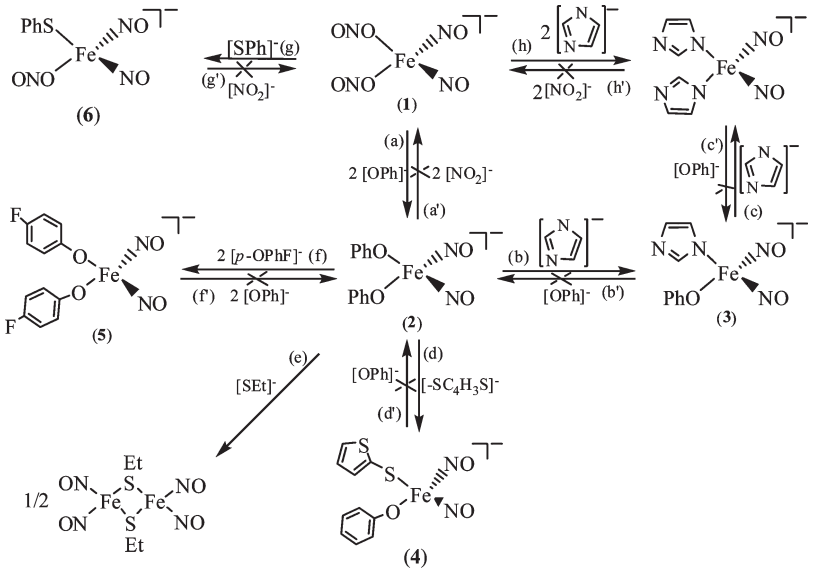

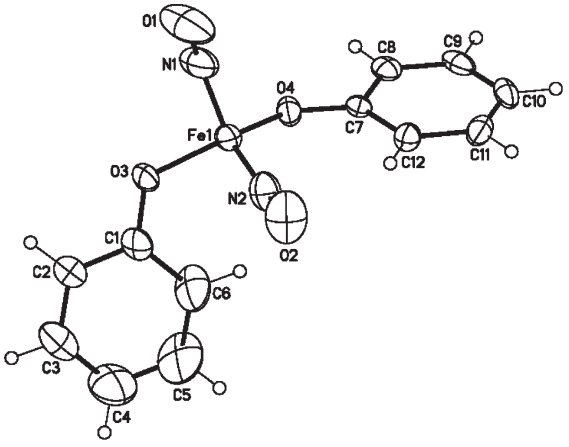

Figure 3. ORTEP drawing and labeling scheme of complex **2** with thermal ellipsoids drawn at 30% probability. Selected bond distances (Å) and angles (deg): Fe(1)−N(1) 1.696(3), Fe(1)−N(2) 1.683(3), Fe(1)−O(3) 1.913(2), Fe(1)−O(4) 1.920(2), N(1)−O(1) 1.177(4), N(2)−O(2) 1.182(4), N(2)−Fe(1)−N(1) 110.2(2), N(1)−Fe(1)−O(3) 104.8(2), N(2)−Fe(1)−O(3) 112.4(1), N(1)−Fe(1)−O(4) 108.3(1), N(2)−Fe(1)−O(4) 114.9(1), O(3)−Fe(1)−O(4) 105.6(1), O(1)−N(1)−Fe(1) 156.4(4), O(2)−N(2)−Fe(1) 164.1(3).

THF solution of complex **1** led to the formation of the anionic $\{Fe(NO)_2\}^9$ [PPN][$(NO)_2Fe(OPh)_2$] (**2**) (yield 85%) with monodentate phenoxide ligands coordinated to the $\{Fe(NO)_2\}^9$ motif (Scheme 1a), characterized by IR, UV−vis, EPR, SQUID, and single-crystal X-ray crystallography (Figure 3). This result seems to follow the rule observed in the previous study that the stronger electron-donating thiolates $[R'S]^-$, compared to the coordinated thiolates of $[(NO)_2Fe(SR)_2]^-$, may promote thiolate−ligand exchange to produce the stable $[(NO)_2Fe(SR')_2]^-$.[7b] The conversion of complex **1** to **2** was monitored by IR (IR ν_{NO} shifting from 1775 s and 1705 s cm^{-1} to 1739 m and 1674 s cm^{-1}) and UV−vis spectra (the intense bands at 510 and 615 nm disappeared, accompanied by the simultaneous formation of the absorption bands at 427, 502, and 657 nm). The EPR spectra (Figure 4) exhibiting a well-resolved five-line EPR signal with a g value of 2.025 (the hyperfine coupling constants $a_{N(NO)} = 2.54$ G) at 298 K and a rhombic signal with $g_1 = 2.041$, $g_2 = 2.022$, and $g_3 = 2.013$ at 77 K are consistent with the formation of complex **2**. The magnetic susceptibility measurement of the powder sample of complex **2** was collected in the temperature range of 2.00−300 K at 5 kG (0.5 T). The net molar magnetic susceptibility (χ_M) increased from 7.47×10^{-4} cm^3 mol^{-1} at 300 K to 8.04×10^{-2} cm^3 mol^{-1} at 2 K. The temperature-dependent effective magnetic moment (μ_{eff}) decreases from 2.058 μ_B at 300 K to 1.141 μ_B at 2 K (Figure S1, Supporting Information). Irreversibly, the formation of complex **1** was not observed upon the addition of 2 equiv of $[NO_2]^-$ to the THF solution of complex **2** (Scheme 1a).

In order to elucidate the reactivity of complex **2** and synthesize dinitrosyliron complexes with mixed imidazolate−phenoxide ligands, the reaction of complex **2** and imidazolate was investigated. Careful injection of 1 equiv of the THF-diluted sodium imidazolate solution ([Na][$C_3H_3N_2$])

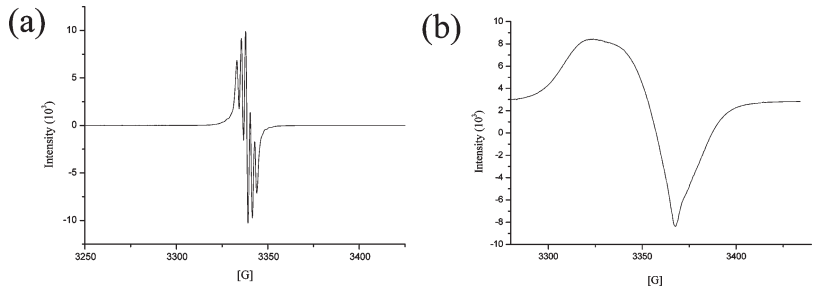

Figure 4. EPR spectrum of complex **2** (a) at 298 K ($g = 2.025$) and (b) at 77 K ($g_1 = 2.041$, $g_2 = 2.022$, and $g_3 = 2.013$) and the simulated EPR spectrum of complex **2** with hyperfine coupling constants of $a_{N(NO)} = 2.54$ G.

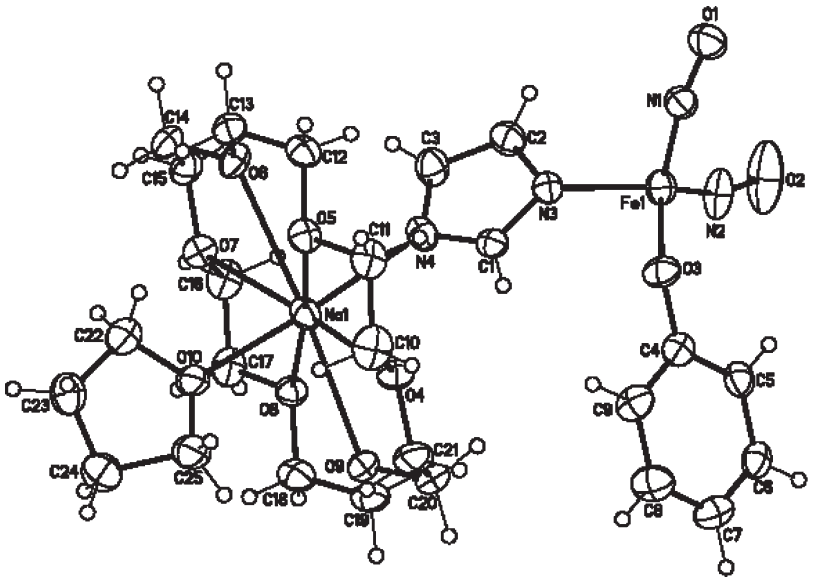

Figure 5. ORTEP drawing and labeling scheme of complex **3-Na** with thermal ellipsoids drawn at 30% probability. Selected bond distances (Å) and angles (deg): Fe(1)−N(1) 1.692(3), Fe(1)−N(2) 1.685(3), Fe(1)−O(3) 1.884(2), Fe(1)−N(3) 1.995(2), N(1)−O(1) 1.173(3), N(2)−O(2) 1.181(3), N(2)−Fe(1)−N(1) 110.5(1), N(2)−Fe(1)−O(3) 119.2(1), N(1)−Fe(1)−O(3) 107.9(1), N(1)−Fe(1)−O(3) 107.9(1), N(3)−Fe(1)−O(3) 101.6(1), N(2)−Fe(1)−N(3) 107.4(1), N(1)−Fe(1)−N(3) 109.8(1), O(1)−N(1)−Fe(1) 164.5(2), O(2)−N(2)−Fe(1) 160.7(3).

into the THF solution of complex **2** at 0 °C led to the IR ν_{NO} stretching frequency shift from 1739 m and 1674 s to 1755 m and 1691 s cm^{-1} (THF), consistent with the ligand displacement of one $[OPh]^-$ yielding [cation][$(NO)_2Fe(OPh)(C_3H_3N_2)$] (cation = PPN (**3-PPN**), Na-18-crown-6-ether (**3-Na**); Scheme 1b). Complex **3-Na** was characterized by single-crystal X-ray crystallography (Figure 5). The UV−vis spectrum of complex **3-Na** shows absorptions at 216 and 270 nm. The EPR spectra (Figure 6) of complex **3-Na** exhibit a nine-line spectrum with $g = 2.026$ (the hyperfine coupling constants $a_{N(NO)} = 2.42$ G and $a_{N(Im)} = 4.15$ G) at 298 K, and a rhombic signal with $g_1 = 2.046$, $g_2 = 2.021$, and $g_3 = 2.013$ at 77 K. However, the addition of 1 equiv of $[OPh]^-$ to complex **3-PPN** in THF shows no spectroscopically detectable changes in the IR and UV−vis spectra (Scheme 1b′). Upon the addition of a second equivalent of the THF-diluted sodium imidazolate to the THF solution of complex **3-Na**, a pronounced color change from dark-brown to red-brown occurs at 0 °C. The IR, UV−vis, EPR, and single-crystal X-ray diffraction studies confirmed the formation of the known anionic $\{Fe(NO)_2\}^9$ $[(NO)_2Fe(C_3H_3N_2)_2]^-$ with two anionic $[C_3H_3N_2]^-$ ligands bound to the $\{Fe(NO)_2\}$ core (Scheme 1c).[12]

The relative binding affinity of the $\{Fe(NO)_2\}$ motif for thienylthiolate/ethylthiolate, compared to phenoxide, nitrite, and imidazolate, was determined through the addition of $[-SC_4H_3S]^-/[SEt]^-$ to the THF solution of complex **2** at 0 °C, respectively. Upon 1 equiv of the THF-diluted sodium thienylthiolate ([Na][$-SC_4H_3S$]) added to the THF solution of complex **2** dropwise at 0 °C, the IR ν_{NO} (1740 s, 1681 s cm^{-1}) suggested the formation of the anionic $\{Fe(NO)_2\}^9$ [PPN][$(NO)_2Fe(OPh)(-SC_4H_3S)$] (**4**; Scheme 1d). At 298 K, complex **4** displays a well-resolved five-line EPR signal with a g value of 2.028 (the hyperfine splitting constant $a_{N(NO)} = 2.58$ G) and a rhombic signal with $g_1 = 2.038$, $g_2 = 2.027$, and $g_3 = 2.013$ at 77 K (Figure 7). However, the addition of 1 equiv of $[OPh]^-$ to complex **4** in THF reveals no detectable changes (Scheme 1d′). This result implicates that the $\{Fe(NO)_2\}$ motif displays a preference for $[-SC_4H_3S]^-$ over $[OPh]^-$. In contrast to the reaction of complex **2** and [Na][$-SC_4H_3S$] leading to complex **4**, the addition of 1 equiv of the THF-diluted $[SEt]^-$ to the THF solution of complex **2** resulted in the formation of the known dinuclear complex [$Fe_2(\mu\text{-}SEt)_2(NO)_4$], characterized by the IR ν_{NO} (shift from 1739 m and 1674 s to 1808 w, 1774 s, and 1749 s cm^{-1}).[17] No detectable quantities of $[(NO)_2Fe(OPh)(SEt)]^-$ were observed spectrally (Scheme 1e). Instead of the formation of the five-coordinate intermediate $[(NO)_2Fe(OPh)_2(-SC_4H_3S)]^{2-}$

(17) Rauchfuss, T. B.; Weatherill, T. D. *Inorg. Chem.* **1982**, *21*, 827–830.

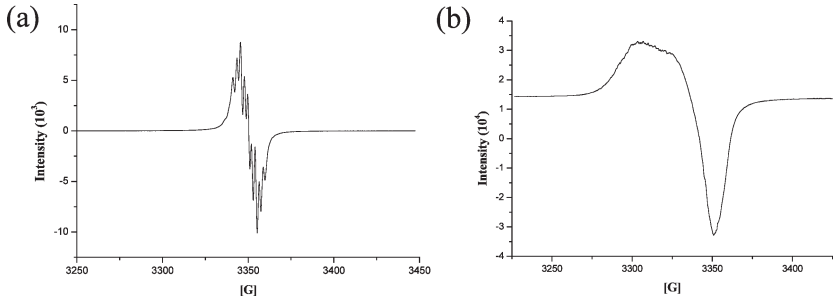

Figure 6. EPR spectrum of complex 3-Na (a) with an isotropic $g_{av} = 2.026$ (a well-resolved nine-line EPR signal) at 298 K and (b) with a rhombic $g_1 = 2.046$, $g_2 = 2.021$, and $g_3 = 2.013$ and the simulated EPR spectrum of complex **3** with hyperfine coupling constants of $a_{N(NO)} = 2.42$ G and $a_{N(Im)} = 4.15$ G.

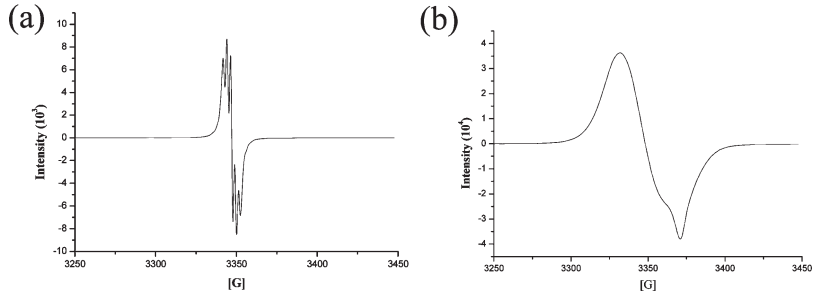

Figure 7. EPR spectrum of complex **4** (a) at 298 K ($g = 2.028$) and (b) at 77 K ($g_1 = 2.038$, $g_2 = 2.027$, and $g_3 = 2.013$) and the simulated EPR spectrum of complex **4** with hyperfine coupling constants of $a_{N(NO)} = 2.58$ G.

Scheme 2

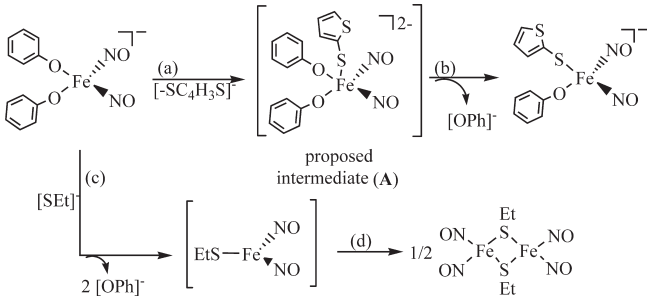

(Scheme 2a,b), it is presumed that a nucleophilic attack of the stronger electron-donating $[SEt]^-$ on complex **2** resulted in the buildup of the unstable three-coordinate intermediate $[(NO)_2Fe(SEt)]$ accompanied by the release $[OPh]^-$, which subsequently dimerized to yield $[Fe_2(\mu\text{-}SEt)_2(NO)_4]$ (Scheme 2c,d).

In order to rationalize the ligand-exchange reactions observed in the above study, the ligand-substitution chemistry of complex **2** with 2 equiv of the analogue $[p\text{-}OPhF]^-$ was also conducted. Transformation of complex **2** into $[PPN][(NO)_2Fe(p\text{-}OPhF)_2]$ (**5**) monitored by IR ν_{NO} spectroscopy (the shift of the ν_{NO} stretching frequencies from 1739 m and 1674 s cm^{-1} to 1751 m and 1685 s cm^{-1}) was observed when a THF solution of complex **2** was reacted with 2 equiv of $[p\text{-}OPhF]^-$ at ambient temperature (Scheme 1f). Complex **5** was characterized by IR, UV−vis, and single-crystal X-ray crystallography (Figure S2, Supporting Information). The EPR spectra (Figure S3, Supporting Information) of complex **5** exhibits a well-resolved five-line signal with $g = 2.026$ (the hyperfine splitting constants $a_{N(NO)} = 2.52$ G) at 298 K and a rhombic signal with $g_1 = 2.041$, $g_2 = 2.024$, and $g_3 = 2.013$ at 77 K. The addition of 2 equiv of $[OPh]^-$ to complex **5** in THF shows no detectable changes in the IR and UV−vis spectra (Scheme 1f′). As expected, the addition of 1 equiv of $[SPh]^-$ into the THF solution of complex **1** yielded $[(NO)_2Fe(SPh)(ONO)]^-$ (**6**), characterized by IR, UV−vis, and single-crystal X-ray crystallography (Scheme 1g), and the reaction of complex **1** with 2 equiv of imidazolate led to the formation of the known $[(NO)_2Fe(C_3H_3N_2)_2]^-$ (Scheme 1h).[12]

The unique ability of the $\{Fe(NO)_2\}$ motif to bind nitrites, phenoxides, and imidazolates as well as thiolates provides the opportunity to directly probe the binding preference of $\{Fe(NO)_2\}$ motif of DNICs. In combination with the previous studies,[7b] the stronger electron-donating thiolates [R′S] promoting thiolate ligand exchange to produce the stable $[(NO)_2Fe(R'S)_2]^-$ and the more electron-donating functionality of thiolates triggering the transformation of $[(NO)_2Fe(C_3H_3N_2)_2]^-$ into complex $[(NO)_2Fe(C_3H_3N_2)(SR)]^-$ (R = ^{t}Bu, Et, Ph) via an imidazolate−thiolate exchange reaction,[12] these results conclude that the binding preference for a given ligand ($[SPh]^-$, $[-SC_4H_3S]^-$, $[C_3H_3N_2]^-$, $[OPh]^-$, and $[NO_2]^-$) of the $\{Fe(NO)_2\}$ motif follows the ligand-displacement series $[SPh]^- \sim [-SC_4H_3S]^- > [C_3H_3N_2]^- > [OPh]^- > [NO_2]^-$ (Scheme 3). This order, presumably, is related to the electronic structure of the $\{Fe(NO)_2\}$ core, an effect that leads to a specific ligand-substitution reaction. The ability of the coordinated ligands to tune the electronic structure of the $\{Fe(NO)_2\}$ core of DNICs affords the optimum electronic conditions to stabilize DNICs. Due to the "homeostasis" of electron density among Fe, NO, and the varieties of coordinating ligands, it is presumed that the electron density surrounding the Fe center of DNICs coordinated by the distinct electron-donating ligands may also be modulated by the noninnocent NO ligands via adjustment of the oxidation level. Although modification of the coordinated ligands in a systematic manner to delineate the electronic structure of the $\{Fe(NO)_2\}$ core is still a challenge, it may be possible to rationalize the preferred formation of thiolate-containing

Scheme 3

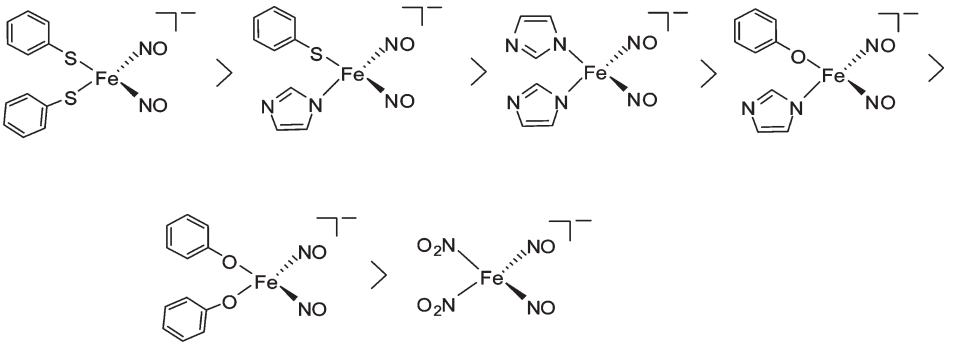

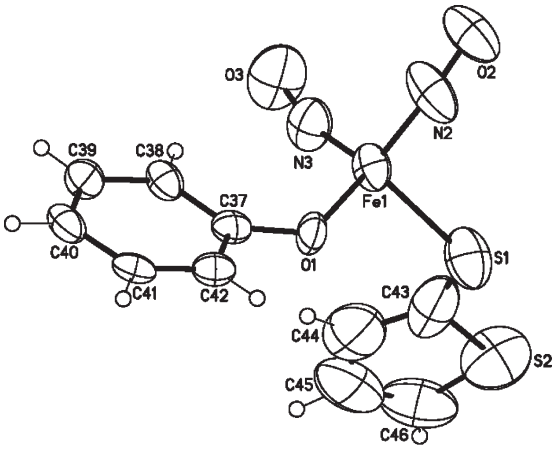

Figure 8. ORTEP drawing and labeling scheme of complex **4** with thermal ellipsoids drawn at 30% probability. Selected bond distances (Å) and angles (deg): Fe(1)−N(2) 1.686(4), Fe(1)−N(3) 1.683(4), Fe(1)−O(1) 1.960(3), Fe(1)−S(1) 2.286(2), N(2)−O(2) 1.144(6), N(3)−O(3) 1.185(5), N(2)−Fe(1)−N(3) 111.9(2), N(3)−Fe(1)−O(1) 115.5(1), N(2)−Fe(1)−O(1) 108.2(1), N(3)−Fe(1)−S(1) 110.6(1), N(2)−Fe(1)−S(1) 104.3(2), O(1)−Fe(1)−S(1) 105.6(1), O(2)−N(2)−Fe(1) 167.3(6), O(3)−N(3)−Fe(1) 164.3(4).

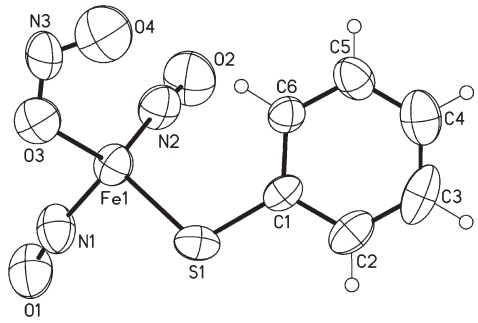

Figure 9. ORTEP drawing and labeling scheme of complex **6** with thermal ellipsoids drawn at 50% probability. Selected bond distances (Å) and angles (deg): Fe(1)−N(1) 1.686(6), Fe(1)−N(2) 1.641(6), Fe(1)−S(1) 2.231(2), Fe(1)−O(3) 2.043(6), N(1)−O(1) 1.157(6), N(2)−O(2) 1.176(6), N(3)−O(3) 1.186(7), N(3)−O(4) 1.100(1), Fe(1)−N(1)−O(1) 162.8(5), Fe(1)−N(2)−O(2) 165.7(5), O(3)−Fe(1)−S(1) 110.8(2).

DNICs via associating a ligand-substitution reaction study with an XAS study of the electronic richness of the $\{Fe(NO)_2\}^9$ core.

Structures. The X-ray crystal structure of complex **1** consists of two crystallographically independent molecules, and the structure of the $[(NO)_2Fe(ONO)_2]^-$ unit in the $[PPN]^+$ salt is shown in Figure 1. The local structure of iron is a distorted tetrahedral geometry with a O(3)−Fe(1)−O(5) bond angle of 93.5(1)°. It is noticed that the O(3)−N(5) and O(5)−N(6) bond lengths of 1.271(2) and 1.303(2) Å in the monodentate O-bound nitrito complex **1**, compared to those of 1.259(4) and 1.263(4) Å in the six-coordinate chelating nitrito $\{Fe(NO)_2\}^9$ DNIC $[(1\text{-MeIm})_2(\eta^2\text{-ONO})Fe(NO)_2]$,[15] are significantly longer than the distal N(5)−O(4) and N(6)−O(6) bond lengths of 1.236(2) and 1.214(2) Å, respectively. The average Fe−NO bond length of 1.695(2) Å falls in the range of 1.661(4)−1.695(3) Å observed in the anionic $\{Fe(NO)_2\}^9$ DNICs.[7d]

Figure 3 displays an ORTEP plot of the anionic $\{Fe(NO)_2\}^9$ complex **2**, and the selected bond distances and angles are listed in the figure caption. The two $[OPh]^-$-coordinate ligands generate a ca. 105.6(1)° O(3)−Fe(1)−O(4) angle. The average N−O bond length of 1.180(4) Å is close to the range of 1.160(6)−1.178(3) Å observed in the anionic $\{Fe(NO)_2\}^9$ DNICs.[7d]

Figure 5 shows the thermal ellipsoid plot of complex **3-Na**, and the selective bond distances and angles are given in the figure captions. The structure of complex **3-Na** can be viewed in terms of the $[(NO)_2Fe(OPh)(C_3H_3N_2)]^-$ anion and the $[C_4H_8O-Na\text{-}18\text{-}crown\text{-}6\text{-}ether]^+$ cation held together by $Na^+\cdots[C_3H_3N_2]^-$ (3′-N of the coordinated depronated imidazole of complex **3-Na**) ionic interaction and the Na^+−O (THF) bond. The shorter Fe(1)−N(3) bond distance of 1.995(2) Å, compared to the reported $Fe-N_{(Im)}$ bond length of 2.021 (4) Å in $[(NO)_2Fe(SC_6H_4\text{-}o\text{-}NHCOPh)(Im)]$ (Im = imidazole),[7c] was attributed to the stronger π-donating ability of the deprotonated imidazole $[C_3H_3N_2]^-$ ligand. The Fe(1)−N(1) and Fe(1)−N(2) bond lengths of 1.692(3) and 1.685(3) Å, respectively, also fall in the range of 1.661(4)−1.695(3) Å observed in the anionic $\{Fe(NO)_2\}^9$ DNICs.[7d] Also, the nearly identical N(1)−O(1) and N(2)−O(2) bond lengths of 1.173(3) and 1.181(3) Å, respectively, are within the range of 1.160(6)−1.178(3) Å observed for the anionic $\{Fe(NO)_2\}^9$ DNICs.[7d]

The structure of the $[(NO)_2Fe(OPh)(-SC_4H_3S)]^-$ unit of complex **4** in $[PPN]^+$ salt is shown in Figure 8. The longer Fe−O(Ph) bond length (1.960(3) Å) in complex **4**, as compared to those of 1.917(2) and 1.884(2) Å in complexes **2** and **3-Na**, respectively, may be attributed to the stronger electronic donation of the $[-SC_4H_3S]^-$ ligand. These results illustrate one aspect of how the distinct electron-donating coordinated ligands positioned near each other in the iron site work in concert to achieve the optimum electronic condition of the $\{Fe(NO)_2\}$ core to stabilize DNICs. Figure S2 (Supporting Information)

Table 1. Selected Bond Distances and IR Vibrational Frequencies of Complexes **1**−**3**, $[(NO)_2Fe(SPh)_2]^-$, $[(NO)_2Fe(C_3H_3N_2)(SPh)]^-$, $[(NO)_2Fe(C_3H_3N_2)_2]^-$, and $[(NO)_2Fe(SEt)_2]^-$ [7e,12]

	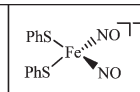	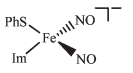	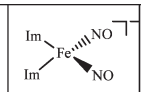	**3**	**2**	**1**	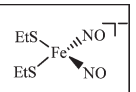
Fe-N (Å)	1.662(4)	1.685(7)	1.686(4)	1.689(3)	1.690(3)	1.695(2)	1.676(6)
N-O (Å)	1.177(5)	1.177(8)	1.172(4)	1.177(4)	1.180(4)	1.173(2)	1.186(7)
Fe-O (Å)	none	2.000(5)	none	1.884(2)	1.917(2)	2.020(1)	none
Fe-S(N) (Å)	2.284(2)	2.265(2)	1.976(3)	1.995(2)	none	none	2.273(2)

displays an ORTEP plot of the anionic complex **5**, and the selected bond distances and angles are listed in the figure caption. Interestingly, the mean Fe−O bond length of 1.916(2) Å (Fe(1)−O(3) = 1.925(1) and Fe(1)−O(4) = 1.906(2) Å) in complex **5** is comparable to that of 1.917(3) Å (Fe(1)−O(3) 1.913(2) and Fe(1)−O(4) = 1.920(2) Å) in complex **2**.

Figure 9 shows the thermal ellipsoid plot of complex **6**, and the selective bond distances and angles are given in the figures' captions. The lengthening of the $Fe-O_{(NO2)}$ bond length (2.043(6) Å) in complex **6**, compared to the $Fe-O_{(NO2)}$ bond length (average 2.020(1) Å) in complex **1**, is presumably caused by electronic perturbation from the stronger electron-donating phenylthiolate-coordinated ligand of complex **6**. Interestingly, the longer Fe−N(O) and N−O bond distances (average 1.695(2) Å and 1.173(2) Å, respectively) of complex **1**, compared to the bond lengths Fe−N(O) (average 1.664(6) Å) and N−O (average 1.167(6) Å) for complex **6**, also reflect the electron deficiency induced by the less electron-donating nitrite-coordinated ligands.

In comparisons with all N−O bond distances of DNICs containing $[ONO]^-$, $[OPh]^-$, $[Im]^-$, $[SEt]^-$, and $[SPh]^-$ coordinated ligands, there are no significant differences within 3σ standard deviations (Table 1). In contrast, the Fe−N bond distances of DNICs shorten from $[ONO]^-$, $[OPh]^-$, and $[Im]^-$ to $[SPh]^-$ (a significant difference of 0.033(4) Å between $[(NO)_2Fe(SPh)_2]^-$ and $[(NO)_2Fe(OPh)_2]^-$). This result may implicate that the highest occupied molecular orbital is dominated by the contributions of the coordinated ligands. This assumption will be further discussed in the MO calculation.

X-Ray Absorption Spectroscopy. The Fe K-edge spectra of a series of reference compounds $[PPN][Fe^{III}(SPh)_4]$, $[PPN]_2[Fe^{II}(SPh)_4]$, and $[PPN][Fe^{III}(OPh)_4]$ are shown in Figure 10a. The pre-edge transition is due to the d−p mixing between Fe and ligand atoms in the distorted T_d local environment of the Fe center.[7a] Taking the apparent peak position of the pre-edge for comparisons, the energy of oxidized form $[Fe(SPh)_4]^-$ shifted from 7113.8 to 7112.5 eV ($[Fe(SPh)_4]^{2-}$) upon one-electron reduction of $[Fe(SPh)_4]^-$. Compared to the tetrahedral Fe(III) complex $[Fe(SPh)_4]^-$, complex $[Fe(OPh)_4]^-$ coordinated by the less covalent phenoxide ligands displaying a higher-rising edge and pre-edge energy at 7114.2 eV may suggest that the effective nuclear charge (Z_{eff}) of Fe in $[Fe(OPh)_4]^-$ is higher than that of $[Fe(SPh)_4]^-$. We noticed that the metal K-edge absorptions are strongly perturbed by the metal oxidation state, coordination geometry, and ligand environment.[18] That is, the energies for these features cannot be used unambiguously as a marker of the oxidation state without an isoleptic reference complex containing an identical coordination geometry. It is interesting to note that the pre-edge energy was known to correlate with the metal oxidation state under the presence of the same coordination geometries and ligand types.[18b] Complexes **1**, **2**, and **5** coordinated by O-containing ligands display the higher pre-edge energies (7113.6, 7113.8, and 7113.7 eV; Figure 10b), compared to those of complexes $[(NO)_2Fe(SEt)_2]^-$ and $[(NO)_2Fe(SPh)_2]^-$ (7113.5 and 7113.5 eV; Figure 10c). Accidentally, we noticed that the pre-edge energies of complexes $[(NO)_2Fe(SEt)_2]^-$, $[(NO)_2Fe(\mu\text{-}SEt)]_2$, and $[(NO)_2Fe(SPh)_2]^-$ (7113.5, 7113.8, and 7113.5 eV) lie between those of complexes $[Fe(SPh)_4]^{2-}$ and $[Fe(SPh)_4]^-$. Also, complexes **1**, **2**, and **5** display the lower pre-edge energies (7113.6, 7113.8, and 7113.7 eV), compared to that of complex $[Fe(OPh)_4]^-$. A list of corresponding pre-edge positions and EPR **g** tensors of iron−nitrosyl complexes is displayed in Table 2, and selected bond distances/angles and spectroscopic data for complexes **1**, **2**, **5**, $[(NO)_2Fe(SPh)_2]^-$, and $[(NO)_2Fe(SEt)_2]^-$ are given in Table 3. As shown in Figure 11, we conclude that the monomeric DNICs containing the varieties of ligation modes exhibit the characteristic pre-edge energy falling in the range of 7113.4−7113.8 eV, in addition to the characteristic EPR signal at $g = 2.03$ ($g = 2.021-2.033$) displayed. Presumably,

(18) (a) DuBois, J. L.; Mukherjee, P.; Stack, T. D. P.; Hedman, B.; Solomon, E. I.; Hodgson, K. O. *J. Am. Chem. Soc.* **2000**, *122*, 5775–5787. (b) Westre, T. E.; Kennepohl, P.; Dewitt, J. G.; Hedman, B.; Hodgson, K. O.; Solomon, E. I. *J. Am. Chem. Soc.* **1997**, *119*, 6297–6314.

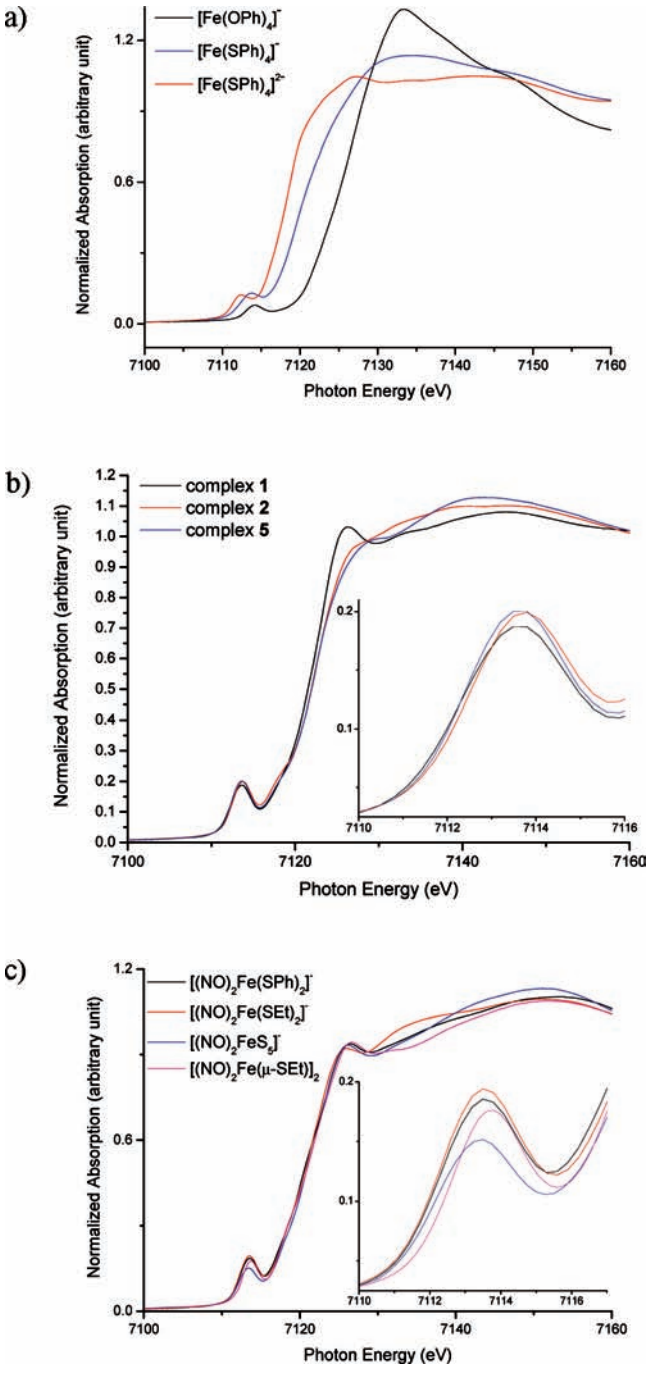

Figure 10. (a) Fe K-edge spectra of complexes $[Fe(OPh)_4]^-$, $[Fe(SPh)_4]^-$, and $[Fe(SPh)_4]^{2-}$. (b) Fe K-edge spectra of complexes **1**, **2**, and **5**, and the pre-edge absorption spectra are enlarged in the inset. (c) Fe K-edge spectra of complexes $[(NO)_2Fe(SPh)_2]^-$, $[(NO)_2Fe(SEt)_2]^-$, $[(NO)_2FeS_5]^-$, and $[(NO)_2Fe(\mu\text{-}SEt)]_2$, and the pre-edge absorption spectra are enlarged in the inset.

in combination with the IR ν_{NO} spectrum, the $\{Fe(NO)_2\}^9$ DNICs featuring the pre-edge energy within the range of 7113.4−7113.8 eV may be adopted to probe the formation of the EPR-silent dimeric DNICs in biological systems.

Computational Study of $[(NO)_2Fe(SEt)_2]^-$, $[(NO)_2Fe(SPh)_2]^-$, and Complex 2. In order to elucidate how the $\{Fe(NO)_2\}^9$ core could be modulated to accommodate the biologically relevant coordination ligands and rationalize the factors contributing to the binding affinity,

Table 2. XAS Pre-edge Energies and Isotropic g-tensor of EPR for Iron Nitrosyl Complexes **1-2, 5**, $[(NO)_2Fe(SEt)_2]^-$ (**6**), $[(NO)_2Fe(SCH_2C(=O)NHCH_3)_2]^-$ (**7**), $[(NO)_2Fe(SPh)_2]^-$ (**8**), $[(NO)_2FeS_5]^-$ (**9**), $[(NO)_2Fe(SePh)_2]^-$ (**10**), $[(NO)Fe(SPh)_3]^-$ (**11**), $[(NO)_2Fe(\mu\text{-}SEt)]_2$ (**12**), $[(NO)_2Fe(\mu\text{-}SEt)]_2^-$ (**13**), $[(1\text{-}MeIm)_2(\eta^2\text{−}ONO)Fe(NO)_2]$ (**14**), $[(NO)Fe(S_2CNEt_2)_2]$ (**15**), $[(NO)Fe(S_2C_6H_4)_2]_3$ (**16**), $[(NO)Fe(S_2C_6H_4)_2]_3^+$ (**17**), $[(NO)Fe(S,S\text{−}C_6H_4)_2]^-$ (**18**)

compound	apparent pre-edge peak	1st derivative ($d\mu/dE = 0$) pre-edge	EPR g_{av}
1	7113.6	7113.6	2.033
2	7113.8	7113.7	2.025
5	7113.7	7113.7	2.026
6	7113.5	7113.6	2.028
7	7113.5	7113.5	2.028
8	7113.5	7113.6	2.028
9	7113.5	7113.4	2.03
10	7113.5	7113.6	2.021
11	7113.0	7113.0	3.76, 2.012
12	7113.8	7113.8	silent
13	7113.4	7113.4	1.997
14	7113.8	7113.7	2.013
15	7113.0	7113.0	2.04
16	7113.4	7113.4	1.999
17	7113.2	7113.2	silent
18	7113.0	7113.0	silent

Table 3. Selected Bond Distances/Angles and Spectroscopic Data for Complexes **1**, **2**, **5**, $[(NO)_2Fe(SPh)_2]^-$, and $[(NO)_2Fe(SEt)_2]^-$ [7e]

complex	**1**	**2**	**5**	$[(NO)_2Fe(SPh)_2]^-$	$[(NO)_2Fe(SEt)_2]^-$
Fe−N(O)	1.695(2)	1.690(3)	1.700(2)	1.662(4)	1.676(6)
N−O	1.173(2)	1.180(4)	1.179(2)	1.177(5)	1.186(7)
∠Fe−N−O	162.7(2)	160.3(4)	161.7(2)	167.2(4)	171.6(6)
∠N−Fe−N	110.3(1)	110.2(2)	110.4(1)	115.1(3)	122.3(3)
IR (cm^{-1}) (THF)	1775, 1705	1739, 1674	1751, 1685	1737, 1693	1715, 1674
$\Delta\nu$ (cm^{-1})	70	65	66	44	41

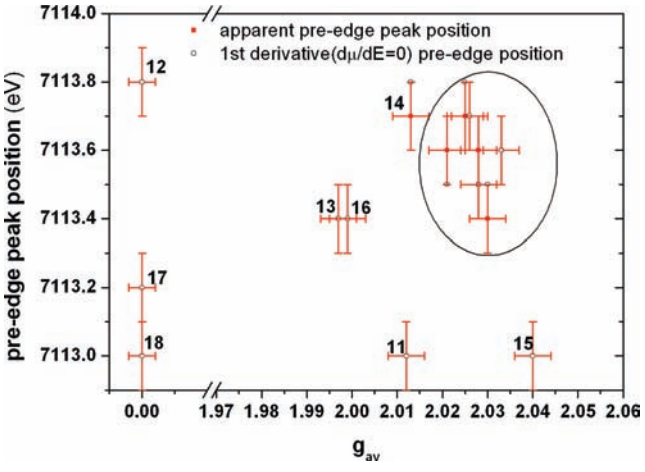

Figure 11. Diagram of XAS pre-edge energy vs isotropic **g** tensor of EPR for complexes **1**, **2**, **5**, $[(NO)_2Fe(SEt)_2]^-$ (**6**), $[(NO)_2Fe(SCH_2C(=O)NHCH_3)_2]^-$ (**7**), $[(NO)_2Fe(SPh)_2]^-$ (**8**), $[(NO)_2FeS_5]^-$ (**9**), $[(NO)_2Fe(SePh)_2]^-$ (**10**), $[(NO)Fe(SPh)_3]^-$ (**11**), $[(NO)_2Fe(\mu\text{-}SEt)]_2$ (**12**), $[(NO)_2Fe(\mu\text{-}SEt)]_2^-$ (**13**), $[(1\text{-}MeIm)_2(\eta^2\text{-}ONO)Fe(NO)_2]$ (**14**), $[(NO)Fe(S_2CNEt_2)_2]$ (**15**), $[(NO)Fe(S_2C_6H_4)_2]_3$ (**16**), $[(NO)Fe(S_2C_6H_4)_2]_3^+$ (**17**), and $[(NO)Fe(S,S\text{−}C_6H_4)_2]^-$ (**18**).

the DFT calculations of $[(NO)_2Fe(SEt)_2]^-$, $[(NO)_2Fe(SPh)_2]^-$, and complex **2** were performed. The initial coordinates of $[(NO)_2Fe(SEt)_2]^-$, $[(NO)_2Fe(SPh)_2]^-$, and

(19) Lu, T.-T.; Tsou, C.-C.; Huang, H.-W.; Hsu, I.-J.; Chen, J.-M.; Kuo, T.-S.; Liaw, W.-F. *Inorg. Chem.* **2008**, *47*, 6040–6050.

complex **2** for geometry optimization with DFT calculations were taken from the crystal structures published in the literatures and this report.[7e,19] As shown in Table 4, the optimized structures of three complexes well reproduce the experimental data with slightly shorter Fe−N and longer N−O bond distances (deviation < 0.02 Å) and Fe−N−O angles (deviation $< 3°$). The calculated vibrational frequencies ν_{N-O} reasonably reproduce the relative trend of $[(NO)_2Fe(SEt)_2]^-$, $[(NO)_2Fe(SPh)_2]^-$, and complex **2** measured in IR spectroscopy (Table 4). The SOMO (singly occupied molecular orbital) of $[(NO)_2Fe(SPh)_2]^-$ and complex **2** are displayed in Figure 12. The atomic contributions of the frontier orbitals are listed in the Supporting Information (Tables S1−S3). Both BP86 and B3LYP functionals indicate that the highest occupied molecular oribtal is dominated by ligands' contributions (87%, 77%, and 86% of ligands SPh, SEt, and OPh for B3LYP; 62%, 56%, and 66% of ligands SPh, SEt, and OPh for BP86, respectively).

Table 4. Experimental and Calculated Data of $[(NO)_2Fe(SEt)_2]^-$, $[(NO)_2Fe(SPh)_2]^-$, and Complex **2**

	IR ν_{NO} (cm^{-1})		X-ray crystal structure (Å)		geometry optimized structure (Å)	
	exptl	calcd	Fe−N	N−O	Fe−N	N−O
$[(NO)_2Fe(SEt)_2]^-$	1674, 1715	1639, 1689	1.676(6)	1.186(7)	1.660	1.198
$[(NO)_2Fe(SPh)_2]^-$	1693, 1737	1674, 1726	1.662(4)	1.177(5)	1.660	1.191
complex **2**	1674, 1739	1680, 1750	1.690(3)	1.180(4)	1.675	1.194

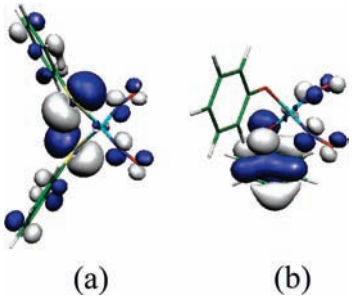

Figure 12. The SOMO of $[(NO)_2Fe(SPh)_2]^-$ and $[(NO)_2Fe(OPh)_2]^-$.

The unexpected trend of Fe−N and N−O bond distances may be interpreted via analysis of bonding interactions. The representive energy diagram of Fe and NO predominant molecular orbitals and the population of selected antibonding molecular orbitals related to the $Fe-N_{NO}$ bonding of $[(NO)_2Fe(SPh)_2]^-$ and complex **2** were shown in Figure 13 and Table 5, respectively, and the corresponding antibonding orbitals of complex **2** are shown in Figure 14. The four lowest-energy unoccupied α spin orbitals and five unoccupied β spin orbitals of $[(NO)_2Fe(SPh)_2]^-$ and complex **2** are predominated by NO $2\pi^*$ and Fe 3d characters, respectively. Bonding characters between Fe and NO evaluated by the corresponding $Fe-N_{NO}$ antibonding orbitals of both α and β spin orbitals are well documented.[20,21] Adopting the extreme electronic structure description of $\{Fe^{III}(NO^-)_2\}^9$, the unoccupied antibonding orbital analysis of the corresponding Fe−NO bond might be able to discriminate the different bonding interactions between Fe and NO.

Table 5. Selected Mulliken Population of the Corresponding Antibonding Orbitals of $[(NO)_2Fe(SPh)_2]^-$ and Complex **2**

$[(NO)_2Fe(SPh)_2]^-$				complex **2**			
	label	%3d	%NO		label	%3d	%NO
α89	$^-\pi_h^*/d_{xy}$[a]	10	89	α81	$^-\pi_h^*/d_{xy}$	9	90
α88	$^-\pi_v^*/d_{yz}$	10	90	α80	$^-\pi_v^*/d_{yz}$	8	92
α87	$^+\pi_h^*/d_{x^2-y^2}$	15	81	α79	$^+\pi_v^*/d_{xz}$	12	83
α86	$^+\pi_v/d_{xz}$	12	76	α78	$^+\pi_h^*/d_{x^2-y^2}$	13	86
β89	d_{xy}_$d_{xz}/^-\pi_h^*$	59	32	β81	$d_{xy}/^-\pi_h^*$	59	33
β88	$d_{x^2-y^2}/^+\pi_h^*$	62	28	β80	$d_{xz}/^+\pi_v^*$	67	21
β87	$d_{xz}/^+\pi_v^*$	56	25	β79	$d_{x^2-y^2}/^+\pi_h^*$	71	24
β86	$d_{yz}/^-\pi_v^*$	54	43	β78	$d_{yz}/^-\pi_v^*$	58	40
β85	$d_{z^2}/^+\pi_h^*$	71	6	β77	$d_{z^2}/^+\pi_h^*$	76	10

[a] The combinations of $(NO)_2$ $2\pi^*$ orbitals are denoted by the following notations: "v" and "h" represent vertical and horizontal to the Fe−N−O plane, respectively. The symbol "+" represents two NO $2\pi^*$ orbitals possessing the symmetry plane which is perpendicular to the N−O−O−N plane, and "−" represents two NO $2\pi^*$ orbitals not possessing the symmetry plane which is perpendicular to the N−O−O−N plane. "$^-\pi_h^*/d_{xy}$" is used to denote an orbital that is a mixture of the $^-\pi_h^*$ and d_{xy} orbitals, and the former represents the larger contribution to the orbital.

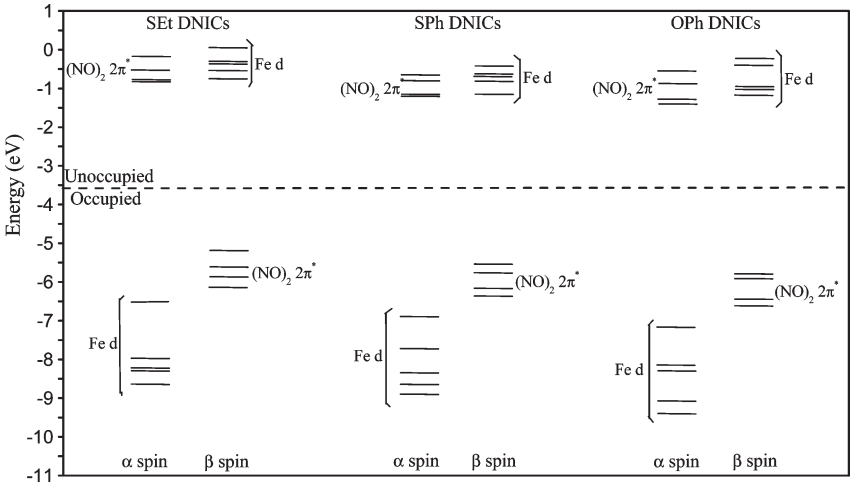

Figure 13. Representive energy level diagram of Fe and NO predominant molecular orbitals for spin-unrestricted calculations of optimized $[(NO)_2Fe(SEt)_2]^-$, $[(NO)_2Fe(SPh)_2]^-$, and complex **2**.

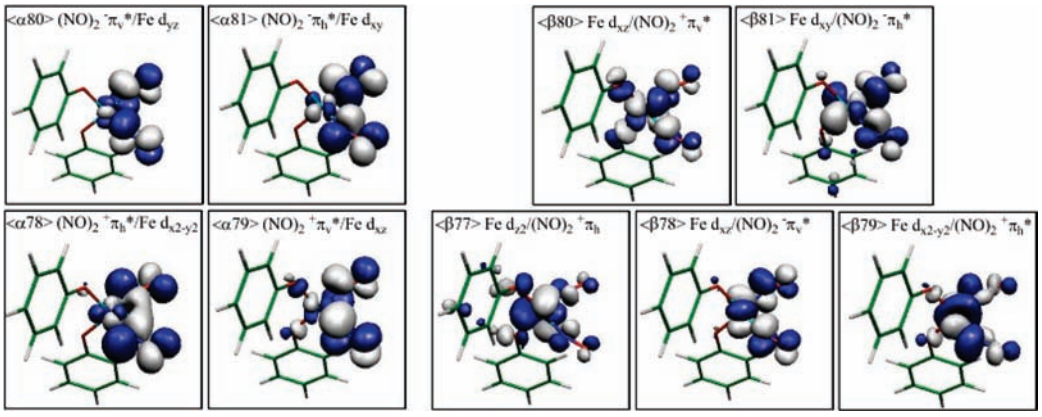

Figure 14. The corresponding antibonding orbitals of complex **2**. The coordinates of those complexes were defined as follows: the *x* axis was chosen as the direction which bisects the N−Fe−N angle within the N−Fe−N plane, the *y* axis was chosen as the direction which roughly passes through two N atoms within the N−Fe−N plane, and the *z* axis was chosen as the direction which is perpendicular to the N−Fe−N plane and orthogonal to the *x* and *y* axes.

Table 6. Selected Natural Charge of $[(NO)_2Fe(SEt)_2]^-$, $[(NO)_2Fe(SPh)_2]^-$, and Complex **2**

natural charge	$[(NO)_2Fe(SEt)_2]^-$	$[(NO)_2Fe(SPh)_2]^-$	complex **2**
Fe	1.00	0.98	1.29
N1	−0.12	−0.10	−0.13
N2	−0.12	−0.10	−0.13
O1	−0.30	−0.27	−0.27
O2	−0.30	−0.27	−0.26

That is, the Fe 3d population in the lowest four unoccupied α spin orbitals represents the back-bonding interactions between the occupied Fe 3d α spin orbitals and the unoccupied NO 2π* α spin orbital. As shown in Table 5, the strengths of back-bonding interactions (summation of Fe 3d population in α corresponding to Fe−N_{NO} antibonding orbitals) for $[(NO)_2Fe(SPh)_2]^-$ are larger than those of complex **2** (47% ($[(NO)_2Fe(SPh)_2]^-$) vs 42% (complex **2**)). The NO population of the corresponding Fe−N_{NO} antibonding orbitals in the β spin manifold represents the donor interactions between the occupied NO 2π* β spin orbitals and the unoccupied Fe 3d β spin orbital. Since no bonding interactions between d_{z^2} and NO 2π* orbitals are found in the bonding orbitals, the strength of donor interactions is estimated by the summation of the NO population in β corresponding to Fe−N_{NO} antibonding orbitals associated with d_{xy}, d_{yz}, d_{xz}, and $d_{x^2-y^2}$ orbitals. Similar to the back-bonding interactions presented in the α spin orbitals, $[(NO)_2Fe(SPh)_2]^-$ also demonstrates the stronger donor interaction in comparison with complex **2** (128% ($[(NO)_2Fe(SPh)_2]^-$) vs 118% (complex **2**)). Overall, the analysis of corresponding Fe−N_{NO} antibonding orbitals demonstrates that $[(NO)_2Fe(SPh)_2]^-$ exhibits the stronger back-bonding and donor interactions compared to those of complex **2**. The NBO charge analysis displayed in Table 6 indicates that the natural charge of Fe (1.29) of complex **2** is significantly more positive than that of $[(NO)_2Fe(SPh)_2]^-$ (0.98) and $[(NO)_2Fe(SEt)_2]^-$ (1.00), which is consistent with the XAS results showing a more electropositive charge of Fe in complex **2** than that in $[(NO)_2Fe(SPh)_2]^-$.

DFT calculation results lead to the proposition that the electronic structure of the $\{Fe(NO)_2\}^9$ core of DNICs might be described as a resonance hybrid of $\{Fe^I(NO)_2\}$ (NBO charge) and $\{Fe^{III}(NO^-)_2\}$ in terms of the extents of donor interactions (dominant) and back-bonding interactions (minor) between Fe and NO ligands. The coordinated phenoxide may polarize the $\{Fe(NO)_2\}^9$ core of complex **2**; that is, the population of the $\{Fe^{III}(NO^-)_2\}$ resonance form in $[(NO)_2Fe(OPh)_2]^-$ is higher than that of thiolate-coordinated $[(NO)_2Fe(SPh)_2]^-$. It implicates that the facile conversion of complex **2** to complex **4** may be rationalized by the preferred formation of five-coordinated intermediate $[(NO)_2Fe(OPh)_2(-SC_4H_3S)]^{2-}$ resulting from the nucleophilic binding of $[-SC_4H_3S]^-$ to the relative electron-deficient Fe center (attributed to the enhancement of $\{Fe^{III}(NO^-)_2\}$ character) of complex **2**. Presumably, the distinct electronic structures of DNICs polarized by the nature of coordinated ligands may elaborate the relative binding affinity of biologically relevant ligands toward the $\{Fe(NO)_2\}^9$ core in the above study.

Conclusion and Comments

Studies on the dinitrosyl iron complexes **1**−**6** containing nitrite-, imidazolate-, phenoxide-, and thiolate-coordinated ligand(s) and the transformations among complexes **1**−**6** and $[(NO)_2Fe(C_3H_3N_2)_2]^-$ have led to the following results, including certain results from earlier studies.[7,12,13]

(1) The anionic $\{Fe(NO)_2\}^9$ DNICs containing the various ligations $[NO_2,NO_2]$/ $[NO_2,SPh]$/$[OPh,OPh]$/$[OPh,SC_4H_3S]$-/$[OPh,C_3H_3N_2]$ were synthesized. The differences in $\{Fe(NO)_2\}$ affinity for thiolates, imidazolate, phenoxide, and nitrite, probed by ligand-substitution reactions, explain the inclusion of the stronger electron-donating thiolate-coordinated ligand producing the more thermally stable $\{Fe(NO)^2\}^9$ DNICs (i.e., $[(NO)_2Fe(SPh)_2]^-$ > $[(NO)_2Fe(SPh)(C_3H_3N_2)]^-$ > $[(NO)_2Fe(C_3H_3N_2)_2]^-$ > $[(NO)_2Fe(OPh)(C_3H_3N_2)]^-$ > $[(NO)_2Fe(OPh)_2]^-$ > $[(NO)_2Fe(ONO)_2]^-$). The preferred formation of thiolate-containing DNICs via a ligand-exchange reaction may be dictated in

(20) (a) Praneeth, V. K. K.; Näther, C.; Peters, G.; Lehnert, N. *Inorg. Chem.* **2006**, *45*, 2795–2811. (b) Fujisawa, K.; Tateda, A.; Miyashita, Y.; Okamoto, K.-I.; Paulat, F.; Praneeth, V. K. K.; Merkle, A.; Lehnert, N. *J. Am. Chem. Soc.* **2008**, *130*, 1205–1213.

(21) (a) Brown, C. A.; Pavlosky, M. A.; Westre, T. E.; Zhang, Y.; Hedman, B.; Hodgson, K. O.; Solomon, E. I. *J. Am. Chem. Soc.* **1995**, *117*, 715–732. (b) Schenk, G.; Pau, M. Y. M.; Solomon, E. I. *J. Am. Chem. Soc.* **2004**, *126*, 505–515. (c) Brown, C. D.; Neidig, M. L.; Neibergall, M. B.; Lipscomb, J. D.; Solomon, E. I. *J. Am. Chem. Soc.* **2007**, *129*, 7427–7438.

part by thermodynamic preferences for the softer donor and the stronger electron-donating ligands.

(2) The $\{Fe(NO)_2\}$ motif coordinated by different ligands ($[SPh]^-$, $[-SC_4H_3S]^-$, $[C_3H_3N_2]^-$, $[OPh]^-$, and $[NO_2]^-$) displays distinct electronic properties (structure) which are cooperatively regulated by the noninnocent NO ligands. That is, presumably, the iron center of DNICs is tailored to minimize the electronic changes accompanying changes in coordinated ligands. This point has received further support in studies of XAS of DNICs containing different ligations, where it was found that the pre-edge energy derived from the 1s → 3d transition in a distorted T_d environment of the Fe center of DNICs is within the range of 7113.4−7113.8 eV for the anionic $\{Fe(NO)_2\}^9$ DNICs ($[(NO)_2FeS_5]^-$ = 7113.4 eV, $[(NO)_2Fe(SEt)_2]^-$ = 7113.5 eV, $[(NO)_2Fe(SPh)_2]^-$ = 7113.5 eV, $[(NO)_2Fe(ONO)_2]^-$ = 7113.6 eV, $[(NO)_2Fe(p\text{-}OPhF)_2]^-$ = 7113.7 eV, $[(NO)_2Fe(OPh)_2]^-$ = 7113.8 eV).[7a]

(3) The stabilization of these $\{Fe(NO)_2\}^9$ DNICs $[(NO)_2Fe(L)(L')]^-$ (L = NO_2, OPh; L′ = NO_2, OPh, SPh, $-SC_4H_3S$, $C_3H_3N_2$) by the particular combinations of thiolates, imidazolate, phenoxide, and nitrite ligation can be attributed to the optimum electronic structures of the $\{Fe(NO)_2\}$ core. The resonance hybrids of $\{Fe^I(NO)(NO)\}^9$, $\{Fe^{II}(NO)(NO^-)\}^9$, and $\{Fe^{III}(NO^-)_2\}^9$ electronic structures may provide an additional mechanism for the adjustment of the charge at the iron site, facilitated by the coordinated ligands. Specifically, an enhancement of the $\{Fe^{III}(NO^-)_2\}$ electronic structure for the O-bound DNICs compared to S-bound DNICs, modulated by the intraelectron transfer among the redox-active Fe center, noninnocent ligand NO, and the coordinated ligands to accommodate the [S,S]/[S,N]/[S,O]/[N,N]/[N,O]/[O,O] ligation modes, was proposed to preserve the $\{Fe(NO)_2\}^9$ electronic core of DNICs.

The binding affinity of ligands ($[SPh]^-$, $[-SC_4H_3S]^-$, $[C_3H_3N_2]^-$, $[OPh]^-$ and $[NO_2]^-$) toward the $\{Fe(NO)_2\}^9$ motif is in the order of $[SPh]^- \sim [-SC_4H_3S]^- > [C_3H_3N_2]^- > [OPh]^- > [NO_2]^-$. The ligand-exchange experiments used in the synthesis of DNICs containing a variety of [S,S]/[S,N]/-[S,O]/[N,N]/[N,O]/[O,O] coordination modes have demonstrated that the $\{Fe(NO)_2\}^9$ motif shows strong preferences for thiolates over imidazolate/phenoxide/nitrite.[12] Our results bridging the ligand-substitution reaction study and XAS study of the electronic richness of the $\{Fe(NO)_2\}^9$ core may point the way to understanding the reasons for nature's choice of combinations of cysteine, histidine, and tyrosine in protein-bound DNICs[1−4,6] and rationalize that most of the DNICs characterized and proposed nowadays are bound to the proteins almost through the thiolate groups of cysteinate/glutathione side chains in biological systems.[5b]

Experimental Section

Manipulations, reactions, and transfers were conducted under nitrogen according to Schlenk techniques or in a glovebox (N_2 gas). Solvents were distilled under nitrogen from appropriate drying agents (diethyl ether from CaH_2, acetonitrile from $CaH_2-P_2O_5$, methylene chloride from CaH_2, methanol from Mg/I_2, and hexane and tetrahydrofuran (THF) from sodium benzophenone) and stored in dried, N_2-filled flasks over 4 Å molecular sieves. Nitrogen was purged through these solvents (including dimethyl formamide (DMF)) before use. Solvent was transferred to the reaction vessel via stainless cannula under positive pressure of N_2. The reagents sodium hydroxide, ferrous dichloride (Aldrich), *p*-flourophenol (Acros), sodium nitrite (Riedel-deHaen), phenol, bis(triphenylphosphoranylidene) ammonium chloride, and 18-crown-6-ether (TCI) were used as received. Complexes $[(NO)_2Fe(SEt)_2]^-$, $[(NO)_2Fe(SCH_2C(=O)NHCH_3)_2]^-$, $[(NO)_2Fe(SPh)_2]^-$, $[(NO)_2FeS_5]^-$, $[(NO)_2Fe(SePh)_2]^-$, $[(NO)Fe(SPh)_3]^-$, $[(NO)_2Fe(\mu\text{-}SEt)]_2$, $[(NO)_2Fe(\mu\text{-}SEt)]_2^-$, $[(1\text{-}MeIm)_2(\eta^2-ONO)Fe(NO)_2]$, $[(NO)Fe(S_2CNEt_2)_2]$, $[(NO)Fe(S_2C_6H_4)_2]_3$, $[(NO)Fe(S_2C_6H_4)_2]_3^+$, and $[(NO)Fe(S,S-C_6H_4)_2]^-$ were synthesized on the basis of the literature reported.[7,15,17] Infrared spectra of the ν_{NO} stretching frequencies were recorded on a PerkinElmer model spectrum One B spectrometer with sealed solution cells (0.1 mm, CaF_2 windows). UV−vis spectra were recorded on a Jasco V-570 spectrometer. Analyses of carbon, hydrogen, and nitrogen were obtained with a CHN analyzer (Heraeus).

Preparation of $[PPN][(NO)_2Fe(ONO)_2]$ (1). Compounds $[PPN][(CO)_3Fe(NO)]$ (0.7070 g, 1 mmol)[22] and $[NO][BF_4]$ (0.2240 g, 2 mmol) were dissolved in THF (10 mL), and then the mixture solution was stirred for 5 min in an ice bath. The resulting suspension was transferred into the flask containing $[PPN][NO_2]$ (1.1690 g, 2 mmol) by cannula under positive N_2 pressure. After being stirred for 1 h at ambient temperature, the mixture solution was filtered through Celite to remove the insoluble solid. The addition of hexane (20 mL) to the filtrate led to precipitation of a dark solid $[PPN][(NO)_2Fe(ONO)_2]$ (**1**) (28%). Diffusion of diethyl ether−hexane into the THF solution of complex **1** led to dark crystals suitable for X-ray diffraction. IR: 1705 s, 1775 s (ν_{NO}) cm^{-1} (THF); 1711, 1782 (ν_{NO}), 1420, 1073 (ν_{O-N-O}) cm^{-1} (KBr). Absorption spectrum (THF) [λ_{max}, nm (ε, M^{-1} cm^{-1})]: 510 (306), 615 (140). Anal. Calcd for $C_{36}H_{30}N_5O_6P_2Fe$: C, 57.87; H, 4.02; N, 9.38. Found: C, 58.50; H, 4.32; N, 9.15.

Preparation of $[PPN][(NO)_2Fe(OPh)_2]$ (2). Complex **1** (0.3735 g, 0.5 mmol) and [Na][OPh] (0.1160 g, 1.0 mmol) were dissolved in THF and stirred for 5 min under a N_2 atmosphere at ambient temperature. The reaction was monitored with FTIR. The IR spectrum (1739 m, 1674 s cm^{-1} (ν_{NO}) (THF)) was assigned to the formation of $[PPN][(NO)_2Fe(OPh)_2]$ (**2**). The resulting mixture was filtered through Celite to remove the insoluble solid. The filtrate was concentrated under a vacuum, and diethyl ether−hexane (10:15 mL) was added to precipitate red-brown solid **2** (yield 0.3574 g, 85%). Diffusion of diethyl ether−hexane into the THF solution of complex **2** at −15 °C for 1 week led to red-brown crystals suitable for single-crystal X-ray diffraction. IR ν_{NO}: 1739 m, 1674 s cm^{-1} (THF). Absorption spectrum (THF) [nm, λ_{max}(M^{-1} cm^{-1}, ε)]: 427 (18512), 502 (11185), 657 (3476). Anal. Calcd for $C_{48}H_{40}FeN_3O_4P_2$: C, 68.52; H, 4.76; N, 4.99. Found: C, 68.97; H, 4.93; N, 5.25.

Preparation of [cation][$(NO)_2Fe(OPh)(C_3H_3N_2)$] ($C_3H_3N_2$ = imidazolate; cation = PPN^+ (3-PPN), Na-18-crown-6-ether (3-Na)). To a stirred solution of complex **2** (0.4205 g, 0.5 mmol) in THF was added a THF solution of sodium imidazolate (0.0450 g, 0.5 mmol) dropwise by syringe at 0 °C. The IR stretching frequencies (1755 m, 1691 s cm^{-1} (ν_{NO}) (THF)) implicated the formation of $[PPN][(NO)_2Fe(OPh)(C_3H_3N_2)]$ (**3-PPN**). The solution was concentrated under a vacuum, and hexane was then added to precipitate the red-brown solid **3-PPN**. Diffusion of hexane into the THF solution of complex **3-Na** (obtained from the reaction of **3-PPN**, $NaBPh_4$, and 18-crown-6-ether) under nitrogen at −15 °C led to red-brown crystals suitable for X-ray diffraction. Complex **3-PPN**. IR ν_{NO}: 1755 m, 1691 s cm^{-1} (THF). Absorption spectrum (THF) [nm, λ_{max}(M^{-1} cm^{-1}, ε)]: 216 (18588), 270 (9097). Anal. Calcd for $C_{21}H_{32}FeN_4NaO_9$: C, 44.77; H, 5.68; N, 9.95. Found: C, 44.41; H, 5.87; N, 9.24.

(22) McBride, D. W.; Stafford, S. L.; Stone, F. G. A. *Inorg. Chem.* **1962**, *1*, 386–388.

Reaction of Complex 3-PPN and [Na][$C_3H_3N_2$]. Complex **3-PPN** (0.4073 g, 0.5 mmol) and [Na][$C_3H_3N_2$] (0.0450 g, 0.5 mmol) were loaded in a 50 mL Schlenk flask and dissolved in THF. The mixture solution was stirred for 5 min at 0 °C. The reaction was monitored by FTIR. The IR spectrum (1776 m, 1712 s cm^{-1} (ν_{NO}) (THF)) suggests the formation of the known [PPN][$(NO)_2Fe(C_3H_3N_2)_2$].[12] The mixture solution was then filtered through Celite to remove the insoluble solid. Hexane was added to precipitate the known red-brown solid [PPN]-[$(NO)_2Fe(C_3H_3N_2)_2$]. IR ν_{NO}: 1776 m, 1712 s cm^{-1} (THF). Absorption spectrum (THF) [nm, λ_{max}(M^{-1} cm^{-1}, ε)]: 326, 716.[12]

Preparation of [PPN][$(NO)_2$Fe(OPh)(−SC_4H_3S)] (4). A THF solution of [Na][−SC_4H_3S] (0.0695 g, 0.5 mmol) was added dropwise into a stirred solution of complex **2** (0.4210 g, 0.5 mmol) in THF at 0 °C. The mixture solution was stirred for 5 min at 0 °C. The IR ν_{NO} stretching frequency (1740 s, 1681 s cm^{-1} (THF)) was assigned to the formation of [PPN][$(NO)_2$-Fe(OPh)(−SC_4H_3S)] (**4**). The resulting mixture was filtered through Celite to remove the insoluble solid, and then hexane was added into the filtrate to precipitate the red-brown solid [PPN][$(NO)_2$Fe(OPh)(−SC_4H_3S)] (**4**) (yield 0.3019 g, 70%). Diffusion of hexane into the THF solution of complex **4** under nitrogen at −15 °C led to red-brown crystals suitable for single-crystal X-ray diffraction. IR ν_{NO}: 1740 s, 1681 s cm^{-1} (THF). Absorption spectrum (THF) [nm, λ_{max}(M^{-1} cm^{-1}, ε)]: 486 (5955), 572 (2146), 806 (233)). Anal. Calcd for $C_{46}H_{38}FeN_3O_3P_2S_2$: C, 63.99; H, 4.41; N, 4.87. Found: C, 63.67; H, 4.83; N, 5.15.

Reaction of Complex 2 and [Na][SEt]. A THF solution (5 mL) of [Na][SEt] (0.0420 g, 0.5 mmol) was injected drop by drop into a THF solution of complex **2** (0.4205 g, 0.5 mmol) under nitrogen at 0 °C. The IR ν_{NO} stretching frequencies shifting from 1739 m and 1674 s cm^{-1} (complex **2**) to 1808 w, 1774 s, and 1749 s cm^{-1} (THF) implicated the formation of the known [$(NO)_2Fe(\mu$-SEt)$]_2$.[17] The mixture solution was filtered through Celite, and the filtrate was concentrated under a vacuum. Hexane was then added to the filtrate to precipitate the known red-yellow [$(NO)_2Fe(\mu$-SEt$)]_2$ (yield 0.0885 g, 50%).

Reaction of Complex 2 and [Na][*p*-OPhF]. Complex **2** (0.4205 g, 0.5 mmol) and sodium *p*-flourophenoxide ([Na][*p*-OPhF]) (0.1340 g, 1.0 mmol) were dissolved in THF (10 mL) and stirred for 5 min under nitrogen at ambient temperature. The reaction was monitored with FTIR. The IR ν_{NO} stretching frequencies shifting from 1739 m and 1674 s cm^{-1} to 1751 m and 1685 s cm^{-1} implicated the formation of [PPN][$(NO)_2Fe(p$-OPhF$)_2$] (**5**). The mixture solution was filtered through Celite, and the filtrate was concentrated under a vacuum. Diethyl ether−hexane (10:15 mL) was then added to precipitate the red-brown solid [PPN][$(NO)_2$-Fe(*p*-OPhF$)_2$] (**5**) (yield 0.2982 g, 68%). Diffusion of diethyl ether−hexane into the THF solution of complex **5** under nitrogen at −15 °C led to red-brown crystals suitable for X-ray diffraction. IR ν_{NO}: 1751 m, 1685 s cm^{-1} (THF). Absorption spectrum (THF) [nm, λ_{max}(M^{-1} cm^{-1}, ε)]: 439 (14347), 509 (2550). Anal. Calcd for $C_{48}H_{38}FeF_2N_3O_4P_2$: C, 65.71; H, 4.33; N, 4.79. Found: C, 65.97; H, 4.12; N, 5.15.

Preparation of [PPN][$(NO)_2$Fe(SPh)(ONO)] (6). The addition of a THF solution (5 mL) of [Na][SPh] (0.0132 g, 0.1 mmol) into a THF solution (5 mL) of complex **1** (0.0747 g, 0.1 mmol) drop by drop under N_2 atmosphere at 0 °C. The resulting mixture was stirred for 15 min and then filtered through Celite to remove the insoluble solid, presumably, [Na][NO_2]. The addition of hexane (15 mL) to the filtrate led to precipitation of dark red solid [PPN][$(NO)_2$Fe(SPh)(ONO)] (**6**). Diffusion of hexane into the THF solution of complex **6** under nitrogen at −15 °C led to red crystals suitable for X-ray diffraction. IR ν_{NO}: 1752 m, 1697 s cm^{-1} (THF); 1739, 1686 (ν_{NO}), 1418, 1070 (ν_{O-N-O}) cm^{-1} (KBr). Absorption spectrum (THF) [λ_{max}, nm (ε, M^{-1} cm^{-1})]: 462 (1900), 759 (365). Anal. Calcd for $C_{42}H_{35}N_4O_4P_2SFe$: C, 62.25; H, 4.32; N, 6.92. Found: C, 62.49; H, 4.39; N, 6.49.

X-Ray Absorption Measurements. All X-ray absorption experiments were carried out at the National Synchrotron Radiation Research Center (NSRRC), Hsinchu, Taiwan. Fe K-edge was recorded at room temperature. For Fe K-edge measurements, the experiments were performed in transmission mode at the BL-17C X-ray Wiggler beamline with a double-crystal Si(111) monochromator. The energy resolution $\Delta E/E$ was estimated to be about 2×10^{-4}. High harmonics were rejected by Rh-coated mirrors. The spectra were scanned from 6.912 to 8.006 KeV using a gas-ionization detector. A reference Fe foil is always used simultaneously for the calibration of photon energy. The first inflection point at 7112.0 eV of the Fe foil spectrum is used for energy calibration. The ion chambers used to measure the incident (I_0) and transmitted (I) photon intensities were filled with a mixture of N_2 and He gases and a mixture of N_2 and Ar gases, respectively.

Crystallography. Crystallographic data of complexes **1**, **2**, **3**, **4**, **5**, and **6** were summarized in Supporting Information Tables S4−S12. The crystals chosen for X-ray diffraction studies measured 0.30 × 0.25 × 0.25 mm for complex **1**, 0.30 × 0.25 × 0.05 mm for complex **2**, 0.30 × 0.10 × 0.10 mm for complex **3**, 0.25 × 0.20 × 0.10 mm for complex **4**, 0.30 × 0.15 × 0.05 mm for complex **5**, and 0.40 × 0.30 × 0.20 mm for complex **6**, respectively. Each crystal was mounted on a glass fiber and quickly coated in epoxy resin. Unit-cell parameters were obtained by least-squares refinement. Diffraction measurements for complexes **1**, **2**, **3**, **4**, **5**, and **6** were carried out on a SMART CCD (Nonius Kappa CCD) diffractometer with graphite-monochromated Mo Kα radiation (λ = 0.71073 Å) and between 1.06 and 28.34° for complex **1**, between 1.36 and 28.31° for complex **2**, between 1.54 and 28.38° for complex **3**, between 1.36 and 28.35° for complex **4**, between 1.68 and 28.28° for complex **5**, and between 1.46 and 25.03° for complex **6**. Least-squares refinement of the positional and anisotropic thermal parameters of all non-hydrogen atoms and fixed hydrogen atoms was based on F^2. A SADABS absorption correction was made.[23] The SHELXTL structure refinement program was employed.[24]

EPR Measurements. EPR measurements were performed at the X-band using a Bruker EMX spectrometer equipped with a Bruker TE102 cavity. The microwave frequency was measured with a Hewlett-Packard 5246 L electronic counter. X-band EPR spectra of complex **1** at 77 K in THF were obtained with a microwave power of 19.678 mW (1.978 mW for complex **2**, 0.171 mW for complex **3**, 20.117 mW for complex **4**, 3.809 mW for complex **5**, and 19.824 mW for complex **6**), a frequency of 9.631 GHz for complex **1** (9.625 GHz for complex **2**, 9.432 GHz for complex **3**, 9.456 GHz for complex **4**, 9.471 GHz for complex **5**, and 9.605 GHz for complex **6**), and a modulation amplitude of 0.80 G at 100 kHz.

Magnetic Measurements. The magnetic data were recorded on a SQUID magnetometer (MPMS5 Quantum Design Company) under a 0.5 T external magnetic field in the temperature range of 2−300 K for complex **2**. The magnetic susceptibility data were corrected with temperature-independent paramagnetism (TIP; 2×10^{-4} cm^3 mol^{-1}) and ligands' diamagnetism with the tabulated Pascal's constants.[25]

Computation Method. All calculations were carried out with the ORCA electronic structure package, version 2.6.63.[26] The coordinates used for geometry optimization were based on the experimental structures taken from the X-ray diffraction

(23) Sheldrick, G. M. *SADABS*; University of Göttingen: Göttingen, Germany, 1996.
(24) Sheldrick, G. M. *SHELXTL*; Siemens Analytical X-ray Instruments Inc.: Madison, WI, 1994.
(25) Kahn, O. *Molecular Magnetism*; VCH: New York, 1993.
(26) Neese, F. *ORCA*, version 2.6.35; University of Bonn: Bonn, Germany, 2008.

experiments.[7e] The geometry optimizations were done in redundant internal coordinates. The BP86 functional together with the aug-cc-pVTZP basis set on the Fe, S, N, and O atoms and SV(P) basis set on the C and H atoms were used in the geometry optimization,[27] and the Coulomb term was approximated with the resolution-of-the-identity (RI) approximation to gain computation efficiency.[28]

The SCF calculations were tightly converged (10^{-7} Eh in energy, 10^{-6} in the density change, and 10^{-6} in maximum element of the DIIS error vector). The geometry search for all complexes was carried out in redundant internal coordinates without imposing symmetry constraints. In all cases, the geometries were considered converged after the energy change was less than 1×10^{-6} Eh; the gradient norm and maximum gradient element were smaller than 1×10^{-4} Eh/Bohr and 3×10^{-5} Eh/Bohr, and the root-mean square and maximum displacements of all atoms were smaller than 6×10^{-4} Bohr and 1×10^{-3} Bohr, respectively. All single-point energy and vibrational frequencies were calculated at the B3LYP level with the same basis sets used in the geometry optimization, and the solvent effect of tetrahydrofuran ($\varepsilon = 7.25$) was treated with the conductor-like screening model (COSMO) as implemented in ORCA.[29] Isosurface plots of the MOs were generated using the Molekel program with an isovalue surface at 0.04 au.[30] The natural population analysis of the B3LYP-level wave function obtained from ORCA calculations was done with the GENNBO package by Weinhold and co-workers.[31]

Acknowledgment. We gratefully acknowledge financial support from the National Science Council of Taiwan and facilities from the National Center for High-Performance Computing. The authors thank Miss Pei-Lin Chen and Mr. Ting-Shen Kuo for the single-crystal X-ray structural determinations and Dr. Tsu-Chien Weng for valuable discussions.

Supporting Information Available: X-ray crystallographic files in CIF format for the structure determinations of $[PPN][(NO)_2Fe(ONO)_2]$, $[PPN][(NO)_2Fe(OPh)_2]$, [Na-18-crown-6-ether]$[(NO)_2Fe(OPh)(C_3H_3N_2)]$, $[PPN][(NO)_2Fe(OPh)(\text{-}SC_4H_4\text{-}S)]$, $[PPN][(NO)_2Fe(p\text{-}OPhF)_2]$, and $[PPN][(NO)_2Fe(SPh)(ONO)]$. Coordinates for optimized geometries. This material is available free of charge via the Internet at http://pubs.acs.org.

(27) (a) Becke, A. D. *Phys. Rev. A* **1988**, *38*, 3098–3100. (b) Perdew, J. P. *Phys. Rev. B* **1986**, *33*, 8822–8824. (c) Schäfer, A.; Horn, H.; Ahlrichs, R. *J. Chem. Phys.* **1992**, *97*, 2571–2577. (d) Eichkorn, K.; Treutler, O.; Öhm, H.; Häser, M.; Ahlrichs, R. *Chem. Phys. Lett.* **1995**, *240*, 283–289. (e) Dunning, T. H. Jr. *J. Chem. Phys.* **1989** *90*, 1007–1023.

(28) (a) Baerends, E. J.; Ellis, D. E.; Ros, P. *Chem. Phys.* **1973**, *2*, 41–51. (b) Dunlap, B. I.; Connolly, J. W. D.; Sabin, J. R. *J. Chem. Phys.* **1979**, *71*, 3396–3402. (c) Vahtras, O.; Almlöf, J. E.; Feyereisen, M. W. *Chem. Phys. Lett.* **1993**, *213*, 514–518.

(29) (a) Andzelm, J.; Kölmel, C.; Klamt, A. *J. Chem. Phys.* **1995**, *103*, 9312–9320. (b) Sinnecker, S.; Rajendran, A.; Klamt, A.; Diedenhofen, M.; Neese, F. *J. Phys. Chem. A* **2006**, *110*, 2235–2245.

(30) Molekel, Advanced Interactive 3D-Graphics for Molecular Sciences. http:www.cscs.ch/molkel/ (accessed September 2009).

(31) Glendening, E. D.; Badenhoop, J. K.; Reed, A. E.; Carpenter, J. E.; Bohmann, J. A.; Morales, C. M.; Weinhold, F. *NBO 5.0*; Theoretical Chemistry Institute, University of Wisconsin: Madison, WI, 2001. http://www.chem.wisc.edu/~nbo5 (accessed September 2009).